Volume 55
Number 8
24 February 2026
Pages 3155-3588

Dalton Transactions

An international journal of inorganic chemistry

rsc.li/dalton

ISSN 1477-9226

ROYAL SOCIETY OF CHEMISTRY

PAPER

Claudia Belviso *et al.*

Upcycled materials for water treatment and emerging contaminant recovery: a preliminary study on waste-derived magnetic zeolites

Dalton Transactions

ROYAL SOCIETY OF CHEMISTRY

PAPER

View Article Online
View Journal | View Issue

Cite this: *Dalton Trans.*, 2026, **55**, 3242

Upcycled materials for water treatment and emerging contaminant recovery: a preliminary study on waste-derived magnetic zeolites

Claudia Belviso, *[a] Veronica Bonadeo, [b] Maura Mancinelli, [c] Maryam Abdolrahimi, [d,e] Alessandro Lascialfari, [f] Francesca Brero, [f] Annalisa Martucci, [c] Giacomo Diego Gatta, [g] Marco Parolini, [h] Davide Peddis, [d,e] Antonio Lettino, [a] Francesco Cavalcante, [a] Lara Gigli, [i] Federica Maraschi [b] and Michela Sturini [b]

This study explores the applicability of magnetic zeolites from industrial waste—specifically fly ash (FA) combined with either synthetic Fe-based nanoparticles (FANPs1 and FANPs2) or red mud (RM) in differing ratios (FA1RM1 and FA4RM1)—for the removal and recovery of emerging water contaminants. FA and RM originate from coal combustion in thermoelectric power plants and alumina extraction from bauxite, respectively. The resulting materials were first assessed for acute toxicity on a freshwater model organism, revealing no acute effects. They were then tested under environmentally relevant conditions for the removal of ofloxacin (OFL), a fluoroquinolone antibiotic selected as a representative water-persistent contaminant. Subsequently, three extraction techniques—ultrasound-assisted extraction (UsAE), microwave-assisted extraction (MwAE), and magnetic hyperthermia-assisted extraction (MhAE)—were applied to recover the adsorbed OFL. All materials exhibited high OFL loading efficiencies (80–95%). Among the extraction techniques, MwAE yielded the highest OFL recovery (>80% for FANPs2 and FA4RM1), while UsAE and MhAE achieved lower efficiencies (up to ~60%), regardless of the adsorbent used. Post-loading and post-extraction characterization studies provided insights into the adsorption mechanism and revealed significant OFL resorption across all zeolite types. Preliminary tests also confirmed the ability of these materials to capture endocrine-disrupting compounds (EDCs), underscoring their potential for water remediation and recovery applications.

Received 14th October 2025,
Accepted 26th December 2025

DOI: 10.1039/d5dt02472b

rsc.li/dalton

1. Introduction

Pharmaceuticals, and antibiotics in particular, are widely used in public health to treat various diseases. However, most of these compounds are only partially metabolized and reach surface waters *via* wastewater at low but potentially toxic concentrations due to their ineffective removal in wastewater treatment plants.[1,2] Among these, antibiotics pose the most serious threat. Their injudicious use, especially in the past, and the following indiscriminate diffusion in ecosystems represent the major reasons for the development of bacterial resistance.[2,3–5] Fluoroquinolone antibiotics (FQs), a broad class of synthetic antibiotics, are especially concerning because up to 80% of administered FQs are discharged into the environment.[6,7]

In the last few years, numerous remediation strategies have been explored to address the presence of pharmaceuticals in aquatic environments, including biodegradation, advanced oxidation processes and adsorption.[1,8–21] Adsorption using natural or synthetic crystalline materials has emerged as a promising and cost-effective technique.[22–28]

Among minerals, zeolites have been extensively studied due to their open framework structures composed of TO_4 tetrahedra (T = Si, Al, *etc.*), which confer high surface area and poro-

[a]*National Research Council – CNR, Roma, Italy. E-mail: claudia.belviso@cnr.it*
[b]*Department of Chemistry, University of Pavia, 27100 Pavia, Italy*
[c]*Department of Physics and Earth Sciences, University of Ferrara, 44122 Ferrara, Italy*
[d]*Department of Chemistry and Industrial Chemistry & INSTM, University of Genova, nM2-Lab, 16146 Genova, Italy*
[e]*Institute of Structure of Matter, National Research Council, nM2-Lab, Via Salaria km 29.300, Monterotondo Scalo 00015 Roma, Italy*
[f]*Department of Physics, University of Pavia, and INFN, 27100 Pavia, Italy*
[g]*Earth Sciences Department, University of Milano, I-20133 Milano, Italy*
[h]*Environmental Science and Policy Department, University of Milano, 20133 Milano, Italy*
[i]*Elettra-Sincrotrone Trieste S.C.p.A., Materials Characterisation X-ray diffraction (MCX) Beamline, Strada Statale 14 – km 163, 5 in AREA Science Park, Basovizza, Trieste, Italy*

sity, making them suitable for capturing a broad range of organic micropollutants, including antibiotics. The performance of natural and synthetic zeolites for remediation of fluoroquinolone-contaminated water has been described in many papers.[29–31] Previous studies have also conducted experiments to analyze the structural distortions due to the presence of antibiotic molecules loaded in the zeolite pores[32] or have focused their attention on the removal of specific fluoroquinolones from wastewater using TiO_2-modified zeolites or TiO_2-sepiolite-zeolite composites.[33,34]

Other researchers have also investigated zeolites for drug delivery[35–37] and pharmaceutical recovery[38,39] applications, highlighting the importance of not only adsorption but also desorption capabilities. Traditional desorption techniques include solvent extraction[40] and thermal treatment,[41] while ultrasound-assisted extraction[42] and microwave-assisted extraction[33] contribute to a greener approach.[43] However, magnetic hyperthermia – widely used in the medical field mainly for cancer treatment[44–46] – has not yet been applied for environmental applications. This technique relies on magnetic materials (*e.g.*, magnetic nanoparticles, which are super paramagnetic at room temperature) that generate localized heating when exposed to an alternating magnetic field, offering a potentially selective, non-invasive strategy for pollutant desorption. Zeolites can also have magnetic properties by adding magnetic nanoparticles during the synthesis process[47–50] or by exploiting the chemical/mineralogical characteristics of some raw materials such as fly ash (FA) and red mud (RM), as described in some of our previous papers.[51,52] Both FA and RM are waste materials resulting from coal combustion in thermal power plants[53] or produced by the caustic leaching process to extract aluminum from bauxite,[54] respectively. Unfortunately, billions of tons of both FA and RM are still landfilled,[53,55–58] thereby constituting a serious environmental problem. Using part of this large amount of waste to produce zeolites with magnetic properties, to be applied for environmental solutions, is in line with the principles of the circular economy and is beneficial for both the environment and the economy.

This study investigates the use of four magnetic zeolitic materials – synthesized from fly ash, red mud, and iron-based nanoparticles – for the adsorption and recovery of the fluoroquinolone antibiotic ofloxacin (OFL) from aqueous solution under environmentally relevant conditions (μg L^{-1} concentrations in freshwater). OFL was selected as a model contaminant due to its widespread environmental occurrence.[59] For OFL recovery, three extraction techniques were tested: ultrasound-assisted extraction (UsAE), microwave-assisted extraction (MwAE), and magnetic hyperthermia-assisted extraction (MhAE) – a technique traditionally used in biomedical applications, but here tested for the first time in an environmental context.

A further novelty of this work lies in the post-loading and post-extraction characterization of the zeolitic materials to gain insight into drug–material interactions, assess structural integrity, and potential OFL resorption. In addition, the loading-extraction approach was preliminarily extended to other micropollutants, such as endocrine-disrupting compounds (EDCs), to evaluate the broader applicability of these materials. Acute toxicity tests using *Daphnia magna* confirmed the ecological safety of the synthesized zeolites. This article shows the results of laboratory tests with potential large-scale applications, which will be evaluated in future experiments.

2. Materials and methods

2.1. Materials

The experiments were performed using fly ash (FA) collected from the thermoelectric power plant of Cerano, Brindisi (Italy), and red mud (RM) from the aluminum extraction area of Podgorica (Montenegro). The chemical compositions of both wastes are displayed in Table S1.

All chemicals were reagent-grade or higher. Sodium hydroxide pellets, formic acid (HCOOH, for ACS analysis), ammonium fluoride (NH_4F, for ACS analysis), water, acetonitrile (ACN), and methanol (MeOH) for LC/MS were purchased from Carlo Erba Reagents (Milano, Italy). Commercial magnetic nanoparticles (MNPs, 637106) were supplied by Merck (Milan, Italy). Ammonia solution (NH_4OH, 30% v/v), hydrochloric acid (HCl 37%), magnesium nitrate hexahydrate ($Mg(NO_3)_2$-$6H_2O$, 97%), ofloxacin (OFL), 17-β-estradiol (E2), 17-α-ethynyl estradiol (EE2), estrone (E1), progesterone (PROG) and testosterone (TST) were supplied by Sigma Aldrich (Milano, Italy).

2.2. Synthesis of magnetic zeolites

The synthesis was carried out as described in our previous papers.[51,52,54] Briefly, the zeolite formation, using fly ash as raw material, is summarized in the following experimental steps: (a) FA and NaOH in a 1 : 1.2 weight ratio were fused at 550 °C for 1 h; (b) the product was cooled and mixed with powdered MNPs; distilled water was finally added to form a mixture; (c) each mixture (solid and solution) was stirred overnight and incubated for 4 days at 60 °C; (e) the solid part was separated by centrifugation and dried for 12 h at 80 °C after being rinsed with distilled water. The sample with the addition of about 6 wt% of MNP fraction was labelled FANPs1; the other with a higher fraction of MNPs (about 12 wt%) was labelled FANPs2.

The zeolites using FA and RM were obtained following the steps described above, but using mixtures of fly ash and red mud in 4 : 1 or 1 : 1 ratio as raw materials, without the addition of external MNPs. The synthetic products were labelled FA4RM1 and FA1RM1, respectively.

2.3. Toxicity tests of synthetic products

The potential acute toxicity of the synthetic products FANPs1 and FA4RM1 was tested on the freshwater cladoceran *Daphnia magna* according to the *Daphnia* sp. Acute Immobilization Test, OECD 202 guideline (OECD, 2004). *D. magna* adults were cultured in commercial mineral water under controlled laboratory conditions, as described in our previous works.[60,61] Acute toxicity tests were performed under static, non-renewal conditions exposing daphnids (*i.e.*, <24 h old individuals) to 0.2 g

L^{-1} FANPs1 and FA4RM1 for 48 h at 20 ± 0.5 °C and a 16 h light/8 h dark photoperiod. The selected concentration reflects a hypothetical residual amount of each material used in the experiments aimed at investigating its capability in the removal of OFL. Five independent replicates, including ten daphnids each, were prepared for each set of experimental conditions. After 48 h of exposure, immobility (*i.e.*, a proxy of death) was monitored. Individuals were considered immobile when they did not swim for over 15 s after a slight stirring of the solutions in which they were exposed. After checking for immobility, the individuals were observed under a Leica Microsystem EZ4 stereoscopic microscope to capture a picture to confirm the ingestion of FANPs1 and FA4RM1.

2.4. OFL loading experiments

OFL loading on FANPs1, FANPs2, FA4RM1, and FA1RM1 was carried out in a batch mode. Weighed amounts of each material (20 and 50 mg) were mixed with 10 mL of tap water enriched with 10 μg L^{-1} OFL. A few microliters of a diluted acid solution (HCl ≈ 1 M) were added to shift the pH from 8–8.3 (native pH) to around 7. The tubes, wrapped in aluminum foil to prevent light-induced drug degradation, were shaken (orbital shaker) at room temperature overnight. Then, the adsorbent was separated with a magnet, and the supernatant was filtered (0.22 μm nylon syringe filter) before HPLC-MS/MS analysis. The loading efficiency (LE%) of each material was calculated using eqn (1):

$$\mathrm{LE}\% = \frac{(m_i - m_{eq})}{m_i} \times 100 \quad (1)$$

where m_i is the initial OFL amount (μg), m_{eq} is the residual amount of OFL in the solution after equilibration (μg), and (m_i − m_{eq}) is the OFL loaded fraction (μg).

2.5. OFL extraction tests

Three different techniques, ultrasound (UsAE), microwave (MwAE), and magnetic hyperthermia (MhAE) assisted extractions, were used for OFL recovery from FANPs1, FANPs2, FA4RM1, and FA1RM1. 5 mL of an aqueous solution of 20% (m/v) magnesium nitrate hexahydrate and 2% (v/v) ammonia was added to the material in a suitable vessel. Each suspension was subjected to the extraction procedures described in sections 2.5.1, 2.5.2, and 2.5.3.

After each treatment, the extracted solution was separated from the adsorbent phase, filtered through a 0.22 μm nylon filter, and neutralized with a few microliters of HCl ≈1 M, before the HPLC-ESI-MS/MS analysis (see section 2.7).

The recovery (R%) step was calculated using eqn (2):

$$R\% = \frac{m_{ex}}{m_l} \times 100 \quad (2)$$

where m_{ex} (μg) is the amount of extracted analyte and m_l (μg) is the loaded analyte amount after equilibration.

2.5.1 Ultrasound extraction procedure (UsAE). Each suspension was treated in an ultrasonic cleaner (VWR, Milan, Italy) for 10, 20, and 30 min, respectively, and the temperature of each suspension was measured after each treatment.

2.5.2 Microwave extraction procedure (MwAE). A Discover SP microwave system, equipped with Synergy™ software (Discover SP® microwave system, CEM S.r.l., Cologno al Serio, Italy), was used for extraction. A Pyrex® tube containing the suspension was placed in the microwave cavity. The irradiation was modulated to reach and maintain a temperature of 120 °C for 10 min. A simultaneous cooling system (PowerMAX) with airflow allowed the continuous removal of latent reaction heat, thus preventing sample overheating.

2.5.3 Magnetic hyperthermia extraction procedure (MhAE). A Magnetherm™ (model NAN201006) system, developed by NanoTherics (Warrington, United Kingdom), was utilized for magnetic hyperthermia experiments. The system was equipped with a 25 mm high-field coil connected to a 200 nF capacitor. The nominal operating frequency of the magnetic field was set at 167.30 kHz, with a magnetic field amplitude of 40 mT. The temperature of the samples was monitored using a fibre optic temperature probe, which has a temperature operating range from 0 °C to 150 °C.

2.6. Preliminary tests on endocrine disrupting compounds (EDCs)

Loading and extraction tests were carried out on a mixture of endocrine-disrupting compounds according to the procedure described in sections 2.4 and 2.5, with minor adjustments to account for the different physicochemical properties of the analytes (50 mg of adsorbent, 10 mL of tap water, hormone concentration of 10 μg L^{-1}, and methanol as the solvent for UsAE, MwAE, and MhAE extractions).

2.7. HPLC-ESI-MS/MS analysis

An Agilent (Cernusco sul Naviglio, Italy) HPLC apparatus 1260 Infinity coupled with an Agilent 6460C MS spectrometer ESI-MS/MS system was used for the determination of ofloxacin and hormones. Quantitative analysis was performed in multiple reaction monitoring (MRM) mode.

For OFL, an Agilent 120 EC-C18 Poroshell column (3 mm × 50 mm, 2.7 μm), thermostated (30 °C) and equipped with a similar guard column, was used. The mobile phase consisted of (A) 0.05% HCOOH and (B) ACN. The starting concentration was 5% B for 0.5 min, which was then increased to 40% B over 8.5 min with a linear gradient, followed by 98% B for 2 min. The flow rate was 0.5 mL min^{-1}, and the injection volume was 20 μL.

For hormones, an Agilent Zorbax Eclipse Plus C18 (2.1 mm × 150 mm, 3.5 μm), thermostated at 30 °C and equipped with a similar guard column, was used. The mobile phase was (A) aqueous NH_4F 1 mM and (B) ACN. The gradient elution started at 30% B, increased to 85% in 3 min, maintained for 8 min, and then further increased to 98% for 2 min. The flow rate was 0.5 mL min^{-1}, and the injection volume was 10 μL.

The initial conditions were restored after an equilibration time of 7 min for both analyses.

The ESI source parameters and MRM conditions for ofloxacin and hormones HPLC-ESI-MS/MS analysis are shown in Tables S2 and S3, respectively.

2.8. Batch-to-batch reproducibility

The loading–extraction procedure was applied to the independently synthesized FANPs1 and FA4RM1 zeolites. For each batch, 20 mg of material were suspended in 10 mL of tap water spiked with 10 μg L^{-1} OFL, as described in section 2.4, and the suspension was subjected to the extraction procedures outlined in section 2.5. OFL recovery (R%) was calculated using eqn (2).

2.9. Explorative reuse tests

Explorative reuse tests were performed using the same methodology described in sections 2.4 and 2.5, maintaining consistency across all experiments.

2.10. Characterization

All the synthetic products were characterized for their mineralogical composition before and after ofloxacin adsorption. X-ray powder diffraction (XRPD) data were collected using a Bruker D8 Advance Da Vinci powder diffractometer (Bruker AXS, Germany) equipped with CuKα radiation and LynxEye XE silicon strip detector. The samples were scanned in continuous mode from 2 to 80° 2θ with a step size of 0.02°2θ and a counting time of 2 s per step. Phase identification was performed using Bruker AXS EVA software (v.5) and refined using the fundamental-parameter approach (TOPAS v.5.0). The unit cell parameters were refined through whole powder pattern fitting using the LeBail method,[62] and structural refinements were performed *via* full-profile Rietveld analysis employing GSAS software[63] along with the EXPGUI graphical interface.[64] The crystallite size was determined using the FWHM (full width at half maximum) data, and the average crystallite sizes (Å) were calculated using the Scherrer equation, which is based on peak width.[65] Structural refinement of the FANP samples was carried out. The Bragg peak profiles were modeled using a pseudo-Voigt function (Thompson–Cox–Hastings), with the peak cutoff set to 0.01% of the peak maximum, employing three Gaussian terms (GU, GV, and GW) and two Lorentzian broadening coefficients (LX and LY), along with an asymmetry contribution. The zero shift, scale factor, and unit cell parameters were refined. The instrumental background was fitted empirically using a Chebyshev polynomial of the first type with 16 variables. Soft restraints were applied initially to the tetrahedral bond distances (1.670 Å) with a tolerance (σ) of 0.04 Å, which were later removed in the final refinement cycles. Finally, atomic coordinates, site occupancy, and isotropic atomic displacement parameters were refined. The synthetic products were also characterized after each regeneration process by XRD analysis performed at the MCX beamline (2)[66] of the ELETTRA-Sincrotrone Trieste S.C.p.A. facility (Basovizza, Trieste, Italy). The diffraction patterns were collected in transmitting geometry, with the capillary kept spinning during the data collection, and using an incident X-ray beam of 15 keV energy. The samples after UsAE, MwAE, and MhAE were mixed with 10% NIST silicon as an internal standard. The data were scanned in the 2θ range of 2.8–35°.

Morphological observations of all the samples were carried out using a field emission scanning electron microscopy apparatus (FE-SEM model Supra 40, ZEISS NTS Gmbh, Oberkochen, Germany), equipped with an energy dispersive spectrometer (EDS), thus enabling observation of the synthetic products at a very high resolution, down to nanometer sizes.

Thermal analysis was performed before and after OFL loading. Thermogravimetric analysis (TGA) and differential thermal analysis (DTA) curves were obtained through the Netzsch STA 409 PC LUXX® (Gerätebau, Germany) simultaneous TG/DTA thermogravimetric balance. Thermal analyses were performed from room temperature (RT) to 900 °C, with a heating rate of 10 °C min^{-1} under constant and controlled synthetic air flow conditions (flow rate 20 mL min^{-1}). Approximately 30 mg of each sample was utilized for the analyses, with alumina (Al_2O_3) acting as the control and standard reference.

Magnetic properties were investigated by measuring field-dependent magnetization loops at 300 K by using a vibrating sample magnetometer (VSM Model 10 – Microsense). The powders were fixed using epoxy resin to prevent any movement during the measurement.

During MhAE, the zeolites were exposed to an alternating magnetic field, causing the embedded magnetic nanoparticles to generate localized heat through Néel relaxation, where the magnetic moments of individual nanoparticles realign with the field, and Brownian relaxation, where the nanoparticles rotate randomly, generating heat through friction with the surrounding medium.[67] High magnetic field strength was employed to enhance the heating efficiency, promoting the desorption of adsorbed ofloxacin from the zeolite and facilitating its extraction.

3. Results and discussion

3.1. Zeolites formed from wastes

3.1.1 Mineralogical characterization by XRD and SEM analyses. X-ray patterns of synthetic products are shown in Fig. 1. Qualitative phase analysis indicates that both FANPs1 and FANPs2 samples are mainly characterized by the presence of zeolite X (FAU topology) and zeolite A (LTA topology). Other identified crystalline phases were magnetite and quartz (Fig. 1a). Fig. 1b displays the XRD patterns of FA4RM1 and FA1RM1, which reveal significant fractions of amorphous/geopolymer material, as indicated by the broad hump between 19 and 37° (2θ).[68] In addition to the amorphous content, the XRD pattern shows the presence of crystalline phases, with peaks corresponding to zeolite A and sodalite. Both samples also contain katoite, calcite, mullite, hematite, and goethite, while quartz is present only in trace amounts (Fig. 1b).

Quantitative phase analysis confirms that the crystalline components of both FANPs1 and FANPs2 primarily consist of 76% zeolite X and 5% zeolite A, besides magnetite. Trace amounts of quartz are also detected, with 3% in FANPs1 and 2% in FANPs2. These findings indicate a polyphasic compo-

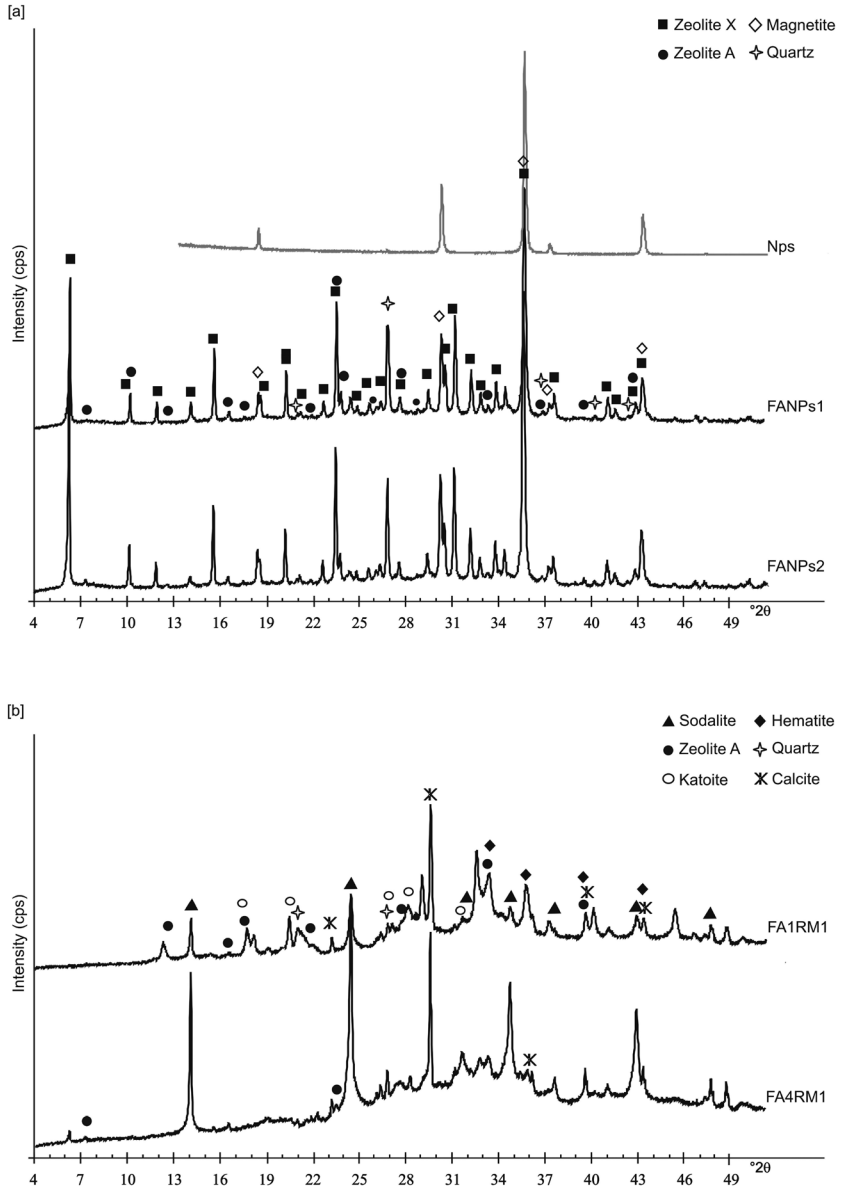

Fig. 1 XRD patterns of FANPs1 and FANPs2 [a] and FA1RM1 and FA4RM1 [b].

sition, with zeolite X being the dominant phase, supplemented by smaller quantities of zeolite A, magnetite, and quartz. In the case of the FA4RM1 and FA1RM1 samples, the XRD analysis reveals that the crystalline part is made up of a significant presence of katoite, amounting to 43% and 42%, respectively. This is followed by zeolite A (10% and 12%), sodalite (9% and 15%), mullite (19% and 20%), hematite (10% and 14%), and quartz (3% and 4%). The presence of katoite and sodalite in these samples is particularly noteworthy, as they represent distinct phases contributing to the overall crystallinity and material properties.

3.1.2. Magnetic characterization. The field-dependent magnetization of the synthetic products at 300 K is presented in Fig. 2. A saturated hysteresis loop, exhibiting both remanent magnetization and coercive fields, is observed in the FANPs1 and FANPs2 samples (Fig. 2a and b). The hysteresis shape of both samples qualitatively matches that of pure synthetic magnetite nanoparticles (Fig. S1), confirming that the magnetic behavior of these samples originates from the incorporated MNPs. The saturation magnetization of FANPs1 (~73 Am^2 kg^{-1}) is lower than that of FANPs2 (~81 Am^2 kg^{-1}), due to the different amounts of magnetic phase. Although the saturation magnetization (M_s) slightly reduced upon incorporation into the fly ash matrix, it remains sufficiently high to respond effectively to an external magnetic field.

On the other hand, the magnetic behavior of the fly ash and red mud composites (FA4RM1 and FA1RM1) (Fig. 2c and d) qualitatively mirrored the magnetic response of pure red mud and fly ash. The sample with a higher proportion of fly ash (FA4RM1) exhibits a saturated hysteresis with a wasp-

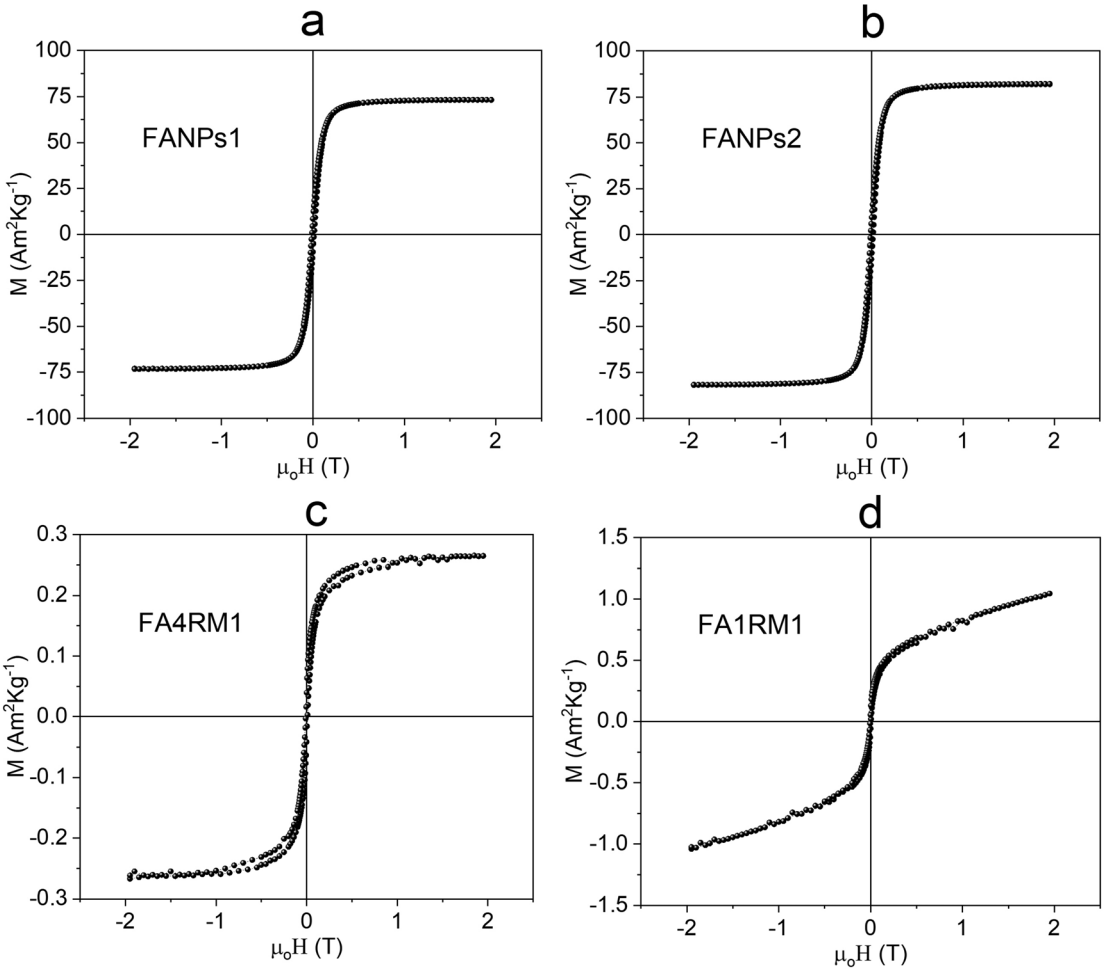

Fig. 2 Field dependence of magnetization recorded at 300 K of the synthetic samples: [a] and [b] fly ash with the addition of different amounts of MNPs; [c] and [d] different ratios of fly ash and red mud combinations.

waisted shape at low fields, attributed to the low red mud content (see Fig. S1a and b). This effect is more pronounced in FA1RM1, which contains a higher proportion of red mud. The magnetic properties of pure fly ash and red mud have been thoroughly investigated in our previous studies.[52,69]

3.1.3. Toxicity test. Daphnids can ingest both FANPs1 and FA4RM1, as demonstrated by the presence of these materials in their digestive tracts (Fig. 3). Despite the ingestion, neither FANPs1 nor FA4RM1 induces acute effects on daphnids. Indeed, the viability at the end of the exposure to the selected concentration of FANPs1 and FA4RM1 was 96.00 ± 8.94% and 92.00 ± 10.95%, respectively, while all the individuals from the control group were alive. The viability of daphnids exposed to FANPs1 and FA4RM1 does not significantly differ from that of the control group (paired Student's *t*-test; for FANPs1: t = 1.000; P = 0.346 and for FA4RM1: t = 1.633; P = 0.140).

3.2. Synthetic product and OFL loading

3.2.1. OFL loading. Loading experiments were designed to replicate environmentally relevant conditions, *i.e.*, tap water, drug concentrations in the microgram-per-liter range, and pH values between 6.5 and 8.0, which are typical pH ranges found in natural freshwater environments. Since tap water has a stable composition like that of natural freshwater, it was used to assess the influence of matrix constituents on drug adsorption. Two adsorbent masses (20 mg and 50 mg) were evaluated for each material, following previous investigations involving other mineral adsorbents.[22,23]

At pH ~8.0–8.3 (native pH), 50 mg of raw FANPs1, FANPs2, and FA4RM1 achieved high OFL loadings ranging from 85(8)% to 93(5)%. In contrast, OFL adsorption onto FA1RM1 was markedly lower, approximately 40(11)%. When pH was adjusted to ~ 6.7–7.0, OFL removal improved across all materials, with efficiencies increasing to 80–95% (Table S4).

This behavior can be explained by considering the dissociation constants of OFL (pK_{a1} = 5.98 and pK_{a2} = 8.00),[7,70] which indicate that the antibiotic mainly exists in positively charged or zwitterionic form within the pH range of 6.5–8.0. Consequently, we may assume that electrostatic interactions between OFL and the zeolite facilitate adsorption. A similar trend was observed when using the lower adsorbent mass (20 mg), as shown in Fig. 4.

Fig. 3 Individuals of *D. magna* from the control group (a) and after exposure to 0.2 g L^{-1} FA4RM1 (b) and FANPs1 (c). Arrows indicate the materials in the digestive tract of daphnids. Scale bar = 500 μm.

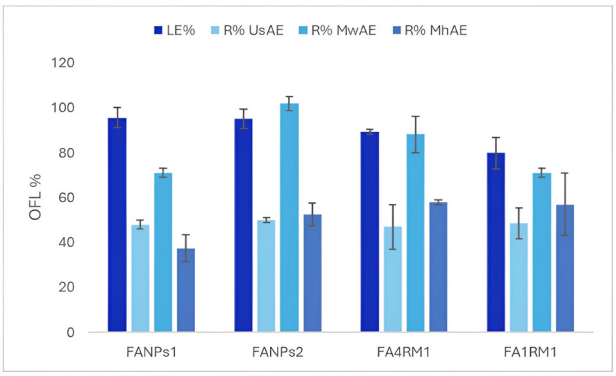

Fig. 4 Results obtained for the zeolitic materials FANPs1, FANPs2, FA4RM1 and FA1RM1 under the selected experimental conditions: OFL loading efficiency (LE%, 20 mg of adsorbent, 10 mL of tap water, OFL 10 μg L^{-1}, n = 6) and OFL recovery by UsAE, MwAE and MhAE (*R%*, 20 mg of adsorbent, 5 mL of extraction solution, 10 min, n = 3).

This methodology demonstrates the feasibility of using these zeolitic materials for the effective removal of fluoroquinolones from water, even at a low dose of 20 mg and in the presence of naturally occurring ions.

3.2.2. Synthetic product characterization after OFL loading. To gain insight into drug–material interactions, further loading experiments were conducted at an antibiotic concentration of 10 mg L^{-1}, corresponding to an effective maximum loading of around 1 mg g^{-1}, in agreement with our previous study[52]. Fig. S2 and S3 display the X-ray profiles of the synthetic products after OFL adsorption at high concentration. The data indicate only slight differences in peak width, which are narrower and exhibit lower intensity after antibiotic treatment of both FANPs1 and FANPs2 synthetic products (Fig. S2). In contrast, samples FA4RM1 and FA1RM1, after loading with OFL, show a reduction in amorphous/geopolymer material, as shown by the XRD patterns in Fig. S3, thus indicating an interaction between the amorphous material and OFL. This result confirms our previous assumptions[52] and suggests that the presence of a porous structure in amorphous geopolymers is responsible for an increase in the sample reactivity.

Structural refinements with the Rietveld procedure were only performed on the FANPs1 and FANPs2 samples, which primarily contain zeolite X (described in the $Fd\bar{3}$ space group).

The refined unit cell parameters, tetrahedral bond distances, and angles do not show significant changes after OFL loading, indicating that the overall framework remains structurally stable. However, small but measurable variations were observed in channel-related parameters such as oxygen–oxygen distances (O1–O1 and O4–O4), crystallographic free area (CFA), and ellipticity (ε, defined as the ratio between the longest and shortest O–O distances) (Table S5). These variations, although subtle, suggest a structural response of the pore system to OFL incorporation and provide direct crystallographic evidence of intrapore adsorption. This interpretation strengthens the adsorption mechanism previously hypothesized for the FAnM material resulting from the combination of fly ash with a low amount of magnetic nanoparticles,[52] where the compatibility between OFL molecular size and zeolite X-type pores was only inferred in the absence of direct structural evidence. In the present study, the observed changes in channel geometry after OFL loading provide crystallographic support for the diffusion of OFL into the internal cavities. The CFA values for FANPs1 and FANPs2 (43.87 and 43.95 $Å^2$, respectively) and the ellipticity values close to unity (0.98 and 1.01) indicate well-preserved, accessible, and nearly circular channels, typical of zeolite X-type structures. These findings support an adsorption mechanism that involves both the external grain surfaces and the internal porosity of FANPs1 and FANPs2. Moreover, the presence of geopolymer amorphous material in both samples is expected to enhance the surface reactivity of the synthetic products toward OFL, in agreement with our previous observations.[52]

Overall, the water content of the zeolite, estimated from the refined occupancies (≈24% in weight), is consistent with the weight loss obtained by thermal analysis (≈20% in weight, up to 900 °C) (Fig. 5). The refined site occupancy indicates that cations are localized within the zeolite channels, along with H_2O molecules (Table S6). Extra-framework cations are bonded to both framework oxygen and H_2O molecules (Table S7). The endothermic reactions observed in the DTA curve, occurring from room temperature up to approximately 150 °C, can be attributed to the desorption of water and OFL molecules weakly bound to the surface. Additional weight loss is observed at temperatures >500 °C, likely due to chemisorbed water, identified as extra-framework species in all samples. The two exothermic peaks at around 275–450 °C and between

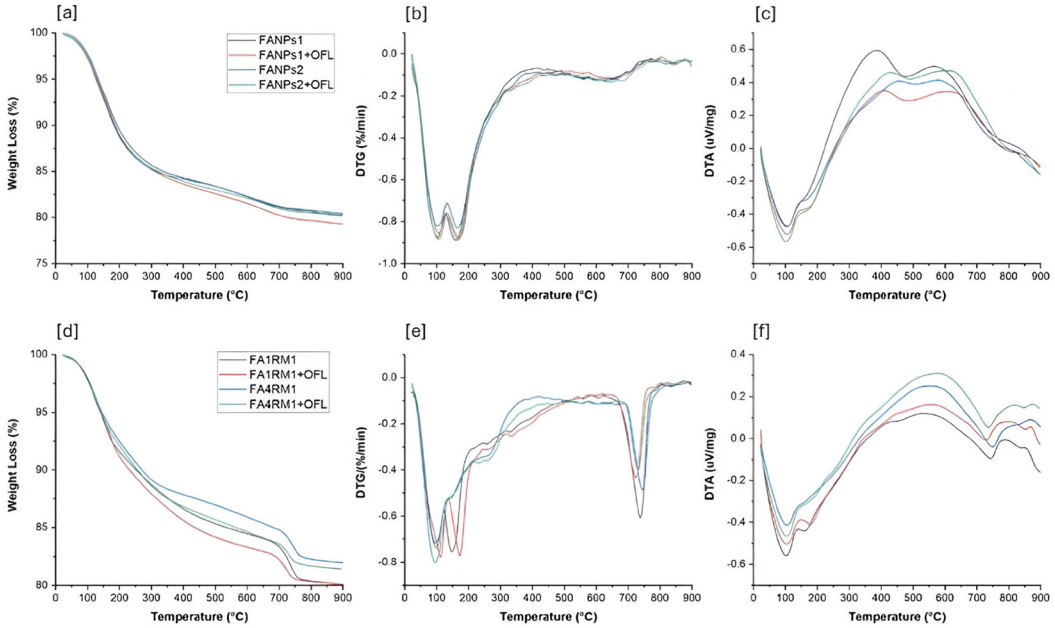

Fig. 5 TG-DTA-DSC plots of FANPs1 and FANPs2 samples (a, b and c) and FA1RM1 and FA4RM1 (d, e and f).

450 and 800 °C indicate the oxidation of the magnetite surface and then of the bulk, respectively. No significant differences in weight loss were observed before and after OFL-loading.

The FA4RM1 and FA1RM1 samples exhibited distinct behavior related to the katoite phase. The initial weight loss, attributed to the desorption of weakly adsorbed H_2O, began immediately upon starting the experiment, resulting in the release of a small amount of water at lower temperatures. As heating continued, mass loss persisted, with water being released through the condensation of hydroxyl groups of katoite in a continuous process between 75 and 900 °C, resulting in an endothermic peak associated with the removal of physically adsorbed H_2O and H_2O from the hydroxyl groups within the structure. Inflections in the TG curve are observed at approximately 110, 250, 410, and 750 °C, corresponding to the minimum in the DTG curves. Considering the successive changes in the slope of the TG curve, water removal occurs in overlapping, sequential steps, with the first step exhibiting the greatest intensity. The endothermic peak around 700 °C corresponds to the loss of any remaining structural H_2O and the onset of phase transitions or decomposition of katoite into different phases, such as anhydrous calcium-aluminum silicates. This peak in the DTA curve occurs at a temperature corresponding also to the Curie point of hematite. Above 700 °C, no notable thermal events are registered on the DTA curve indicating the absence of further phase transitions.

SEM analysis of FANPs1 and FANPs2 samples after enrichment with OFL at 10 mg L^{-1} concentration (effective maximum loading of around 1 mg g^{-1}) still confirms the presence of X-type zeolite as the main crystalline phase (Fig. 6). However, EDX data indicate the absence (or very low presence) of Na in the chemical composition of the synthetic products (Fig. 6 and Fig. S4) compared to the samples before OFL loading (Fig. S5a). This observation may be explained by a possible cation-exchange process between the extra-framework Na^+ cations—introduced during synthesis—and the protonated amine group of the piperazine ring of the zwitterionic antibiotic. On the other hand, electrostatic interactions between the deprotonated carboxylic acid group and mobile Na^+ cations within the pore network cannot be excluded, in line with the zwitterionic nature of the molecule. Similar behavior is observed in FA4RM1 and FA1RM1 samples, although to a lesser extent. According to Belviso *et al.*,[52] adsorption mainly occurs on the external surfaces of the grains rather than within the internal porous structures.

3.3. OFL extraction from synthetic products

3.3.1. OFL extraction tests. Due to the high stability of the FQ–Mg^{2+} complex[71] and the results from our previous studies on similar matrices,[72] hexahydrate magnesium nitrate and ammonia aqueous solution were selected for OFL extraction.

Fig. 4 shows the antibiotic recovery obtained under different experimental conditions.

The ultrasound extraction efficiency for 10 minutes was approximately 50% across all materials, with more significant variability observed for FA4RM1(47(10)%) and FA1RM1(49 (7)%) compared to FANPs1(48(2)%) and FANPs2 (50(1)%) (Table S8). No apparent difference in *R*% was observed when the treatment time was increased to 20 and 30 min, despite the suspension temperature increasing by 6–8 °C for each step.

The effect of temperature was also investigated with MwAE. The results show improved OFL recovery by increasing the extraction temperature from 60 °C to 120 °C. Specifically, at 120 °C, FANPs1 exhibits a slightly lower extraction efficiency

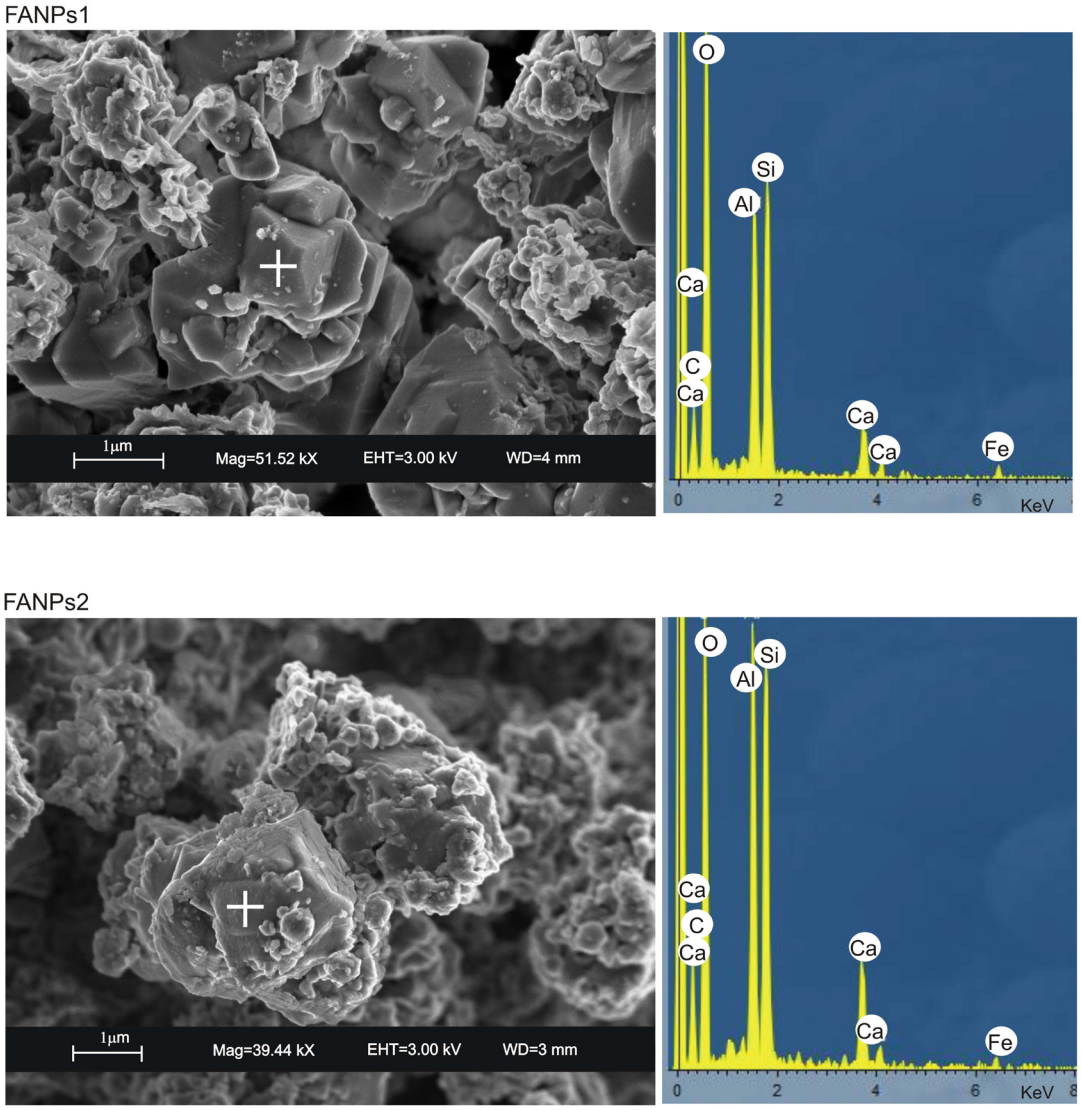

Fig. 6 SEM images and EDX spectrum of FANP samples after OFL loading.

(71(2)%) than FANPs2 (102(3)%), as well as FA1RM1 (71(2)%) when compared to FA4RM1 (88(8)%) (Table S9). At 60 °C, the *R* % of the four zeolitic materials ranges from 54% to 57%.

As the study was not conducted on humans, there were no concerns regarding patient safety (*e.g.*, Brezovich's criterion).[73,74] MhAE experiments were performed at a field strength of 40 mT with extraction time varying from 7 to 15 minutes. Longer extraction times did not significantly affect OFL recovery, which ranged from 40 to 60% across all materials (Table S10). For this reason, the extraction time was set to 10 minutes. The effective heating, detected throughout the experiment, at 10–15 °C for FANPs1 and FANPs2, and 2–4 °C for FA4RM1 and FA1RM1, did not lead to quantitative antibiotic recovery. This agrees with the values of M_s obtained by magnetization measurements that are, of course, higher for samples containing commercial magnetite.

Overall, the differences in extraction efficiency reflect the distinct modes of energy transfer associated with each technique and their resulting capability to weaken the strong host–guest interactions within the zeolite framework.

3.3.2. Zeolite characterization after OFL extraction. To extract OFL from synthetic products (after loading), conventional processes such as ultrasonic and microwave techniques and the unconventional hyperthermia method (used up to now only in the medical field) were used, and XRD analysis was performed on the samples after these processes. The data show that the crystalline structure of the newly formed zeolites is still preserved after all three treatments (Fig. S6).

The crystalline phase composition remains stable in the UsAE, MwAE, and MhAE treated samples, exhibiting no significant changes in phase content. However, slight variations in crystallite size were observed. The FANPs1 and FANPs2 samples showed only marginal differences, while the FA4RM1

and FA1RM1 samples displayed larger crystallites, as indicated in Table S11. Structural refinements with the Rietveld procedure on the FANPs1 and FANPs2 samples do not show marked changes, also after extraction treatments (Tables S5 and S12). The channel geometry remained substantially unchanged (Table S13). This finding indicates that the extraction treatments do not affect the structural integrity of the zeolite framework.

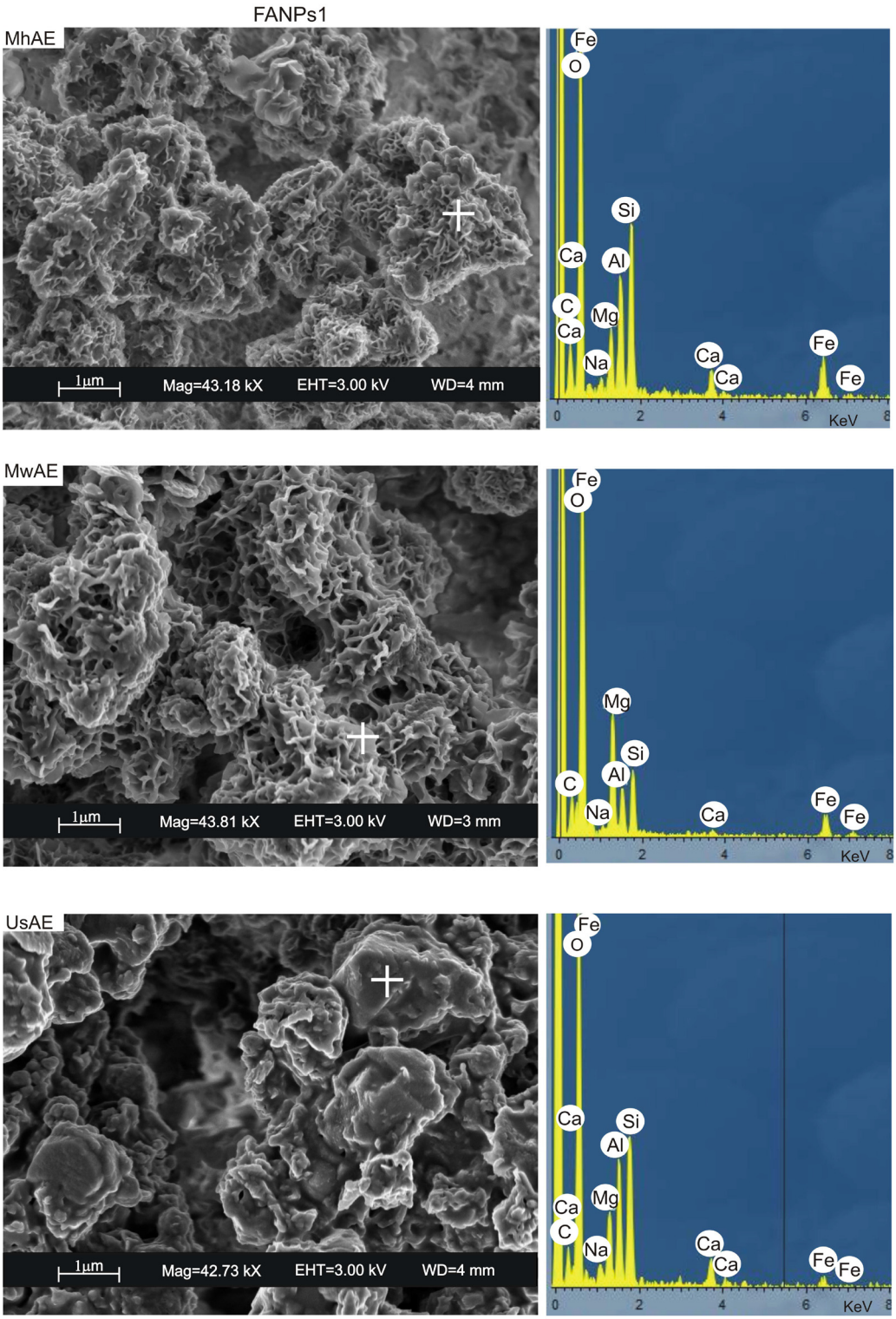

Fig. 7 SEM images and EDX spectrum of FANPs1 after UsAE, MwAE and MhAE treatments.

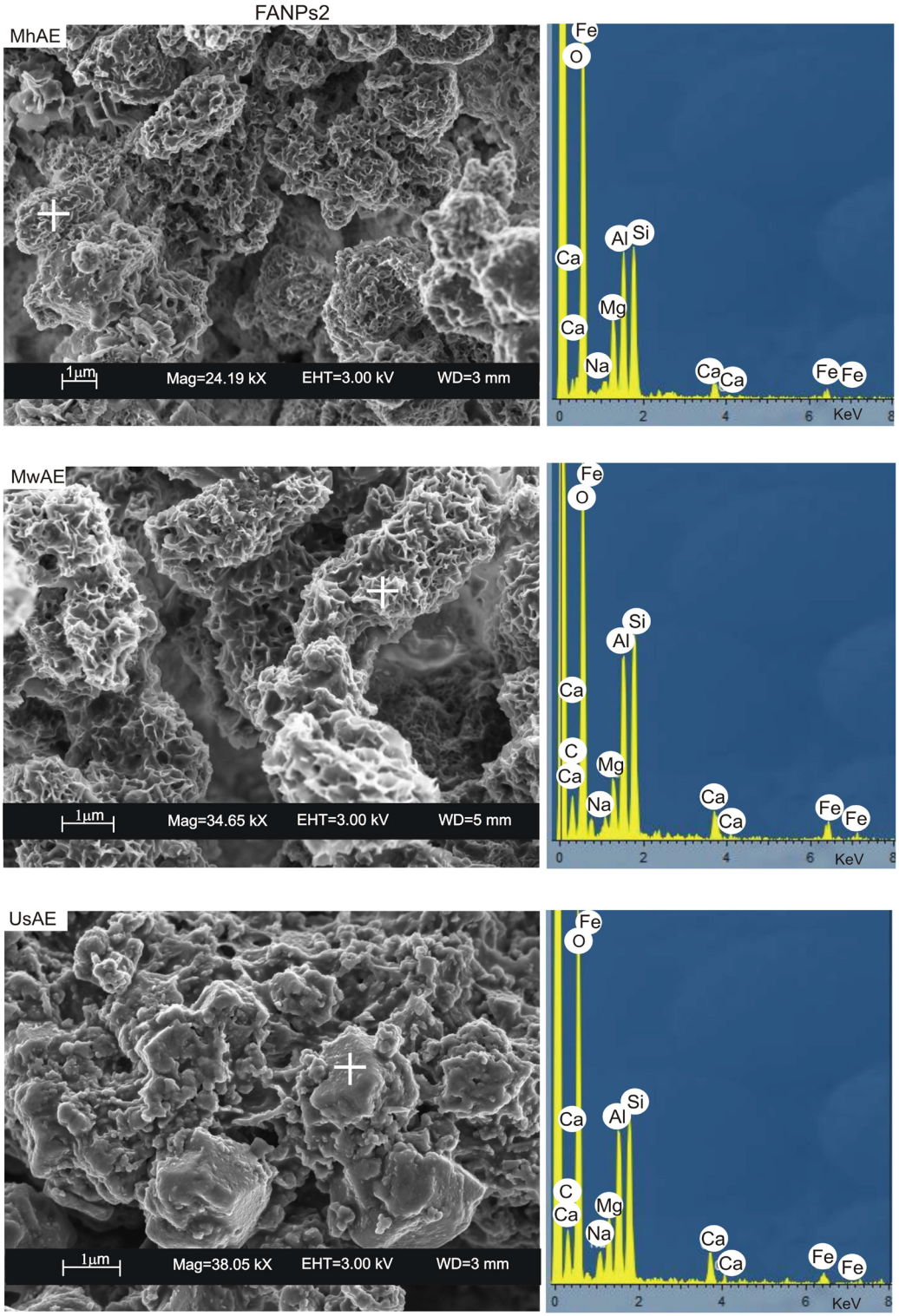

Fig. 8 SEM images and EDX spectrum of FANPs2 after UsAE, MwAE and MhAE treatments.

However, although only weak differences in mineralogical composition are detected among the treated samples, it is interesting to note differences in morphology resulting from each treatment (UsAE, MwAE, and MhAE) in both FANP samples. SEM images in Fig. 7 and 8 show zeolite crystals with irregular surfaces because of the initial dissolution/amorphization process after ultrasonic treatment, probably due to the cavitation bubbles caused by sonication. In contrast, the

surface of the samples after microwave and magnetic hyperthermia treatments is characterized by a diffuse presence of sheets and plates (Fig. 7 and 8). We hypothesize that the local increase in temperature, caused by both MwAE and MhAE, is responsible for the development of interconnected nanostructures (nanograss layers) and nanoflower morphology made of aluminum oxide and metal oxides (magnetic nanoparticles),[75–79] also resulting from the interaction with hot water.[80,81]

As expected, EDX data after UsAE, MwAE, and MhAE indicate the absence of Na and the clear presence of Mg (Fig. 7 and 8 and Table S14), due to the extraction phase used for the antibiotic desorption based on the Mg^{2+} salt. These results corroborate the high cation exchange ability of the synthetic products.

The combined effect of temperature and magnetic phases, as a result of MwAE and MhAE treatments on the morphology of synthetic products, is also confirmed in the FA4RM1 and FA1RM1 samples. These samples exhibit a diffuse, plate-like morphology after exposure to microwave and magnetic hyperthermia (Fig. 9), which is not detected in the samples before the treatments (Fig. S5b). The XRD profiles are presented in Fig. S7. Also, for these samples, EDX data after UsAE, MwAE, and MhAE indicate the absence of Na and the presence of Mg (Table S14).

3.3.3. Batch-to-batch reproducibility. The results, in terms of OFL recovery (R%), from two independent batches of FANPs1 and FA4RM1 are consistent, as shown by percentage standard deviations (<10% for MwAE, 15% for UsAE, and 16–18% for MhAE). This confirms the reproducibility of the entire process, from material synthesis to loading and extraction steps, as detailed in Table S15.

3.3.4. Explorative reuse tests. As the results indicated FANPs1 and FA4RM1 to be more efficient in OFL adsorption, the potential reusability of these samples was preliminarily investigated through explorative loading tests. Specifically, 20 mg of each material was separately suspended in 10 mL of tap water spiked with 10 μg L^{-1} OFL overnight. After this first loading cycle, the materials were recovered and directly subjected to a second OFL loading cycle under the same conditions.

In parallel, an additional set of experiments was conducted to evaluate the effect of regeneration. After the first loading cycle, the materials were separated from the solution and regenerated using the three extraction techniques: UsAE, MwAE, and MhAE. The regenerated materials were then reused in a second OFL loading cycle.

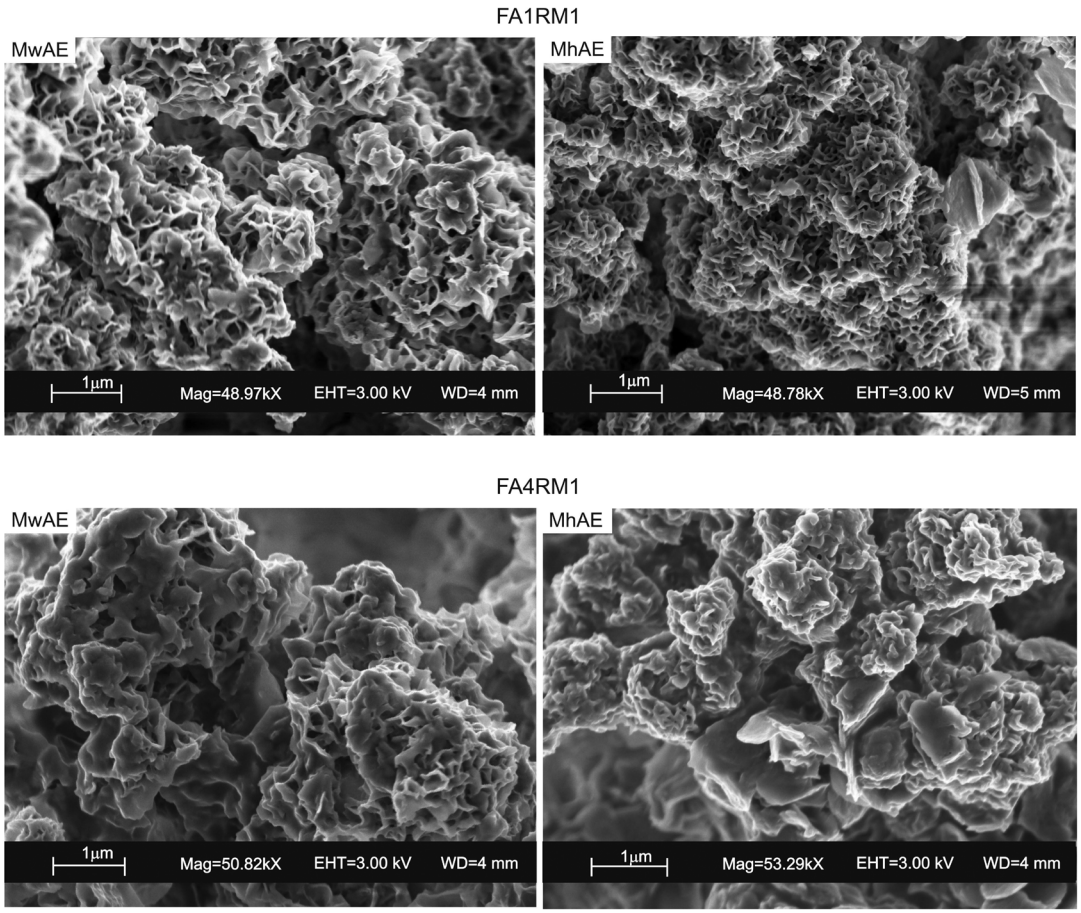

Fig. 9 SEM images of FA1RM1 and FA4RM1 after MwAE and MhAE treatments.

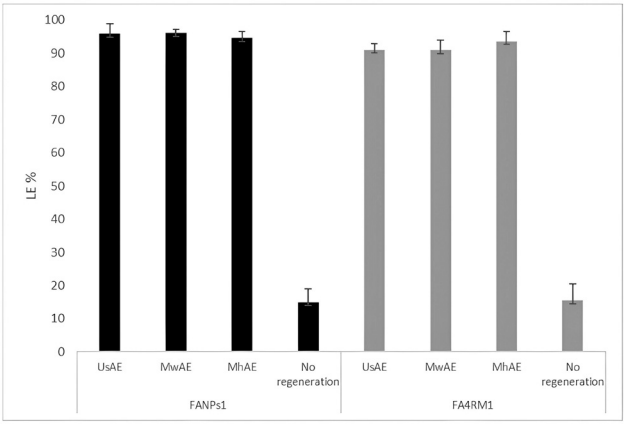

Fig. 10 OFL loading efficiency (LE%) of FANPs1 and FA4RM1 after regeneration by UsAE, MwAE, MhAE, and without regeneration (20 mg of adsorbent, 10 mL of tap water, OFL 10 μg L^{-1}, n = 3).

Fig. 10 shows the OFL R% from FANPs1 and FA4RM1 after the second loading cycle, both with and without regeneration.

Without regeneration, both materials exhibited a marked reduction in adsorption capacity, with OFL removal efficiencies dropping to approximately 15%. In contrast, the regenerated materials exhibited significantly enhanced performance, removing 91–96% of OFL from the solution, regardless of the iron precursor used in synthesis (FA or RM) or the extraction method applied for regeneration. The improved performance following regeneration may be related to the interconnected nanostructures and the nanoflower morphology characterizing the samples, particularly evident after MwAE and MhAE treatments, as detailed in section 3.3.2.

3.4. Preliminary tests on other unconventional contaminants: endocrine disrupting compounds (EDCs)

Based on the promising results obtained with the OFL antibiotic, explorative tests were conducted in the presence of a mixture of endocrine-disrupting compounds.

The loading efficiency of 50 mg of FANPs1, FANPs2, FA4RM1, and FA1RM1 was tested in the presence of 10 μg L^{-1} EDCs in a mixture, namely 17-β-estradiol (E2), 17-α-ethynyl estradiol (EE2), estrone (E1), progesterone (PROG) and testosterone (TST) (Table 1).

EDCs were efficiently loaded onto the zeolitic materials within a few minutes. The LE%, calculated using eqn (1), ranged from 72% to 99%. In particular, FANPs1 and FANPs2 ensured significant loading of E2, EE2, E1, PROG (93–99%), and TEST >80%. FA4RM1 and FA1RM1 were equally efficient (83–96%) for E2, EE2, E1, and PROG, and slightly less efficient for TEST >70%.

Table 1 Loading efficiency (LE%) of FANPs1, FANPs2, FA4RM1 and FA4RM1 (50 mg of adsorbent, 10 mL of tap water, 10 μg L^{-1} EDC, n = 4)

	LE% (sd)				
Adsorbent	E2	EE2	TST	E1	PROG
FANPs1	96 (3)	95 (5)	84 (4)	93 (4)	97 (1)
FANPs2	99 (1)	97 (2)	85 (2)	94 (2)	98 (1)
FA4RM1	96 (4)	89 (3)	73 (12)	84 (10)	96 (1)
FA1RM1	91 (10)	86 (8)	72 (7)	83 (7)	96 (2)

As for the experiments with OFL, UsAE, MwAE, and MhAE were investigated and compared for analyte desorption. MeOH was used as the extractive solvent,[82] and analyses were carried out by HPLC-ESI-MS/MS.

UsAE allowed a good recovery (75–95%) of E2 and E1 from FANPs1, FANPs2, and FA4RM1. In the case of MwAE, EDC extraction efficiencies were 72–115% with FANPs1. FANPs2 was the best-performing material for MhAE, with EDC recovery ranging from 67 to 91%. The less efficient zeolite was FA1RM1, regardless of the extraction technique.

Although no detailed structural refinement was carried out in this case, the high loading efficiency observed for all EDCs suggests strong interaction with the surface of the zeolitic and geopolymeric phases. Given that the molecular dimensions of the studied EDCs (approximately 10–13 Å) are likely too large to allow diffusion through the 12-membered ring channels of X-type zeolites (aperture ~7.4–8.0 Å), adsorption is expected to occur mainly on the external surfaces, within the entrances of large supercages, or in the more accessible amorphous geopolymeric domains. The rapid adsorption kinetics and high LE% values observed in all samples—especially FANPs1 and FANPs2—support this interpretation.

These preliminary results highlight the potential of these materials for removing and recovering endocrine-disrupting compounds in water remediation applications.

4. Conclusion

The data demonstrate that all the zeolites synthesized from waste raw materials are effective in removing OFL from polluted aqueous solutions. Moreover, the adsorbed antibiotic can be efficiently extracted and quantified by different assisted extraction techniques: ultrasonic-assisted extraction (UsAE, ~50% recovery), conventional microwave-assisted extraction (MwAE, exceeding 80% recovery), and magnetic hyperthermia extraction (MhAE, ~60% recovery). These findings suggest that the investigated synthetic materials are promising candidates for the quantitative determination of OFL in polluted water. The practical applicability of these materials is further enhanced by their magnetic properties due to the higher content of magnetic nanoparticles, which facilitate the rapid and easy separation of the sorbents from treated solutions.

Moreover, all regenerated materials after UsAE, MwAE, and MhAE treatments show improved OFL removal efficiency (91–96%) compared to untreated samples, confirming their potential for reuse in water remediation. Finally, the investigated materials were found to be non-toxic to *D. magna*, at the concentrations applied in the removal experiments, supporting their environmental safety. Preliminary investigations on unconventional contaminants, such as endocrine-disrupting

compounds (EDCs), reveal a removal trend consistent with that observed for OFL. This suggests that the synthesized zeolites and associated extraction methods hold significant potential for the removal and recovery of a broad range of emerging contaminants from polluted waters.

Conflicts of interest

There are no conflicts to declare.

Data availability

The data supporting this article have been included as part of the supplementary information (SI). Supplementary information is available. See DOI: https://doi.org/10.1039/d5dt02472b.

References

1 R. Andreozzi, M. Raffaele and P. Nicklas, Pharmaceuticals in STP effluents and their solar photodegradation in aquatic environment, *Chemosphere*, 2023, **50**, 1319–1330.
2 R. Rosato, F. Castellani, M. Ricci, A. Manucci, V. D. Simone, G. Scortichini and G. Saluti, Antibiotics in the aquatic environment. A deep voyage across chemical occurrence data, socio-economic relationships and international policies on antimicrobial consumption and resistance within 2014–2024, *Sci. Total Environ.*, 2025, **1002**, 180543.
3 *World health statistics 2018: monitoring health for the SDGs, sustainable development goals*, World Health Organization, Geneva, 2018, License: CC BY-NC-SA 3.0 IGO.
4 Y. Ben, C. Fu, M. Hu, L. Liu, M. H. Wong and C. Zheng, Human health risk assessment of antibiotic resistance associated with antibiotic residues in the environment: a review, *Environ. Res.*, 2019, **169**, 483–493.
5 M. Bilal, S. Mehmood, T. Rasheed and H. M. Iqbal, Antibiotics traces in the aquatic environment: persistence and adverse environmental impact, *Curr. Opin. Environ. Sci. Health*, 2020, **13**, 68–74.
6 P. Chen, L. Blaney, G. Cagnetta, J. Huang, B. Wang, Y. Wang, S. Deng and G. Yu, Degradation of ofloxacin by perylene diimide supramolecular nanofiber sunlight-driven photocatalysis, *Environ. Sci. Technol.*, 2019, **53**, 1564–1575.
7 X. Van Doorslaer, J. Dewulf, H. Van Langenhove and K. Demeestere, Fluoroquinolone antibiotics: an emerging class of environmental micropollutants, *Sci. Total Environ.*, 2014, **500**, 250–269.
8 K. A. Robberson, A. B. Waghe, D. A. Sabatini and E. C. Butler, Adsorption of the quinolone antibiotic nalidixic acid onto anionexchange and neutral polymers, *Chemosphere*, 2006, **63**, 934–941.
9 H. Dolliver, S. Gupta and S. Noll, Antibiotic degradation during manure composting, *J. Environ. Qual.*, 2008, **37**, 1245–1253.
10 E. A. Serna-Galvis, K. E. Berrio-Perlaza and R. A. Torres-Palma, Electrochemical treatment of penicillin, cephalosporin, and fluoroquinolone antibiotics via active chlorine: evaluation of antimicrobial activity, toxicity, matrix, and their correlation with the degradation pathways, *Environ. Sci. Pollut. Res.*, 2017, **24**, 23771–23782.
11 M. Kamagate, A. A. Assadi, T. Kone, S. Giraudet, L. Coulibaly and K. Hanna, Use of laterite as a sustainable catalyst for removal of fluoroquinolone antibiotics from contaminated water, *Chemosphere*, 2018, **195**, 847–853.
12 B. Yang, L. Meng and N. D. Xue, Removal of five fluoroquinolone antibiotics during broiler manure composting, *Environ. Technol.*, 2018, **39**, 373–381.
13 M. Ateia, D. E. Helbling and W. R. Dichtel, Best practices for evaluating new materials as adsorbents for water treatment, *ACS Mater. Lett.*, 2020, **2**, 1532–1544.
14 J. Q. Ding, Y. He, P. C. Wang, Y. C. Zhou, H. Q. Zhang, B. J. Lin, Z. Wei, M. S. Huang and R. Weng, Performances of simultaneous removal of trace-level ofloxacin and sulfamethazine by different ozonation-based treatments, *J. Cleaner Prod.*, 2020, **277**, 124120.
15 B. L. Phoon, C. C. Ong, M. S. M. Saheed, P. L. Show, J. S. Chang, T. C. Ling, S. S. Lam and J. C. Juan, Conventional and emerging technologies for removal of antibiotics from wastewater, *J. Hazard. Mater.*, 2020, **400**, 122961.
16 D. Capsoni, G. Guerra, C. Puscalau, F. Maraschi, G. Bruni, F. Monteforte, A. Profumo and M. Sturini, Zinc based metal-organic frameworks as ofloxacin adsorbents in polluted waters: ZIF-8 vs. Zn3 (BTC)2, *Int. J. Environ. Res. Public Health*, 2021, **18**, 1433.
17 X. L. Weng, W. L. Cai, G. Owens and Z. L. Chen, Magnetic iron nanoparticles calcined from biosynthesis for fluoroquinolone antibiotic removal from wastewater, *J. Cleaner Prod.*, 2021, **319**, 128734.
18 G. Dong, B. Chen, B. Liu, L. J. Hounjet, Y. Cao, S. R. Stoyanov, M. Yang and B. Zhang, Advanced oxidation processes in microreactors for water and wastewater treatment: Development, challenges, and opportunities, *Water Res.*, 2022, **211**, 118047.
19 L. Leng, L. Wei, Q. Xiong, S. Xu, W. Li, S. Lv, Q. Lu, L. Wan, Z. Wen and W. Zhou, Use of microalgae based technology for the removal of antibiotics from wastewater: a review, *Chemosphere*, 2020, **238**, 124680.
20 B. O. Orimolade, A. O. Oladipo, A. O. Idris, F. Usisipho, S. Azizi, M. Maaza, S. L. Lebelo and B. B. Mamba, Advancements in electrochemical technologies for the removal of fluoroquinolone antibiotics in wastewater: A review, *Sci. Total Environ.*, 2023, **881**, 163522.
21 J. Bednárek, L. Matejová, I. Koutník, M. Vráblová, G. J. F. Cruz, T. Strasák, P. Siler and J. Hrbác, Revelation of high–adsorption-performance activated carbon for removal

of fuoroquinolone antibiotics from water, *Biomass Convers. Biorefin.*, 2024, **14**, 2585–2599.

22 E. Rivagli, A. Pastorello, M. Sturini, F. Maraschi, A. Speltini, L. Zampori, M. Setti, L. Malavasi and A. Profumo, Clay minerals for adsorption of veterinary FQs: Behavior and modelling, *J. Environ. Chem. Eng.*, 2014, **2**, 738–744.

23 M. Sturini, A. Speltini, F. Maraschi, A. Profumo, S. Tarantino, A. F. Gualtieri and M. Zema, Removal of fluoroquinolone contaminants from environmental waters on sepiolite and its photo-induced regeneration, *Chemosphere*, 2016, **150**, 686–693.

24 G. Tian, X. Hua, K. Nie, Y. Li, K. Zhang, W. Qu, H. Ren and J. Meng, Lamellar mesoporous Mg-containing silicate adsorbents derived from iron ore tailings for high-efficient adsorption of mycotoxins and antibiotics, *Sep. Purif. Technol.*, 2024, **330**, 125556.

25 R. Antonelli, F. R. Martins, G. R. P. Malpass, M. G. C. da Silva and M. G. A. Vieira, Ofloxacin adsorption by calcined Verde-lodo bentonite clay: Batch and fixed bed system evaluation, *J. Mol. Liq.*, 2020, **315**, 113718.

26 D. Capsoni, P. Lucini, D. M. Conti, M. Bianchi, F. Maraschi, B. De Felice, G. Bruni, M. Abdolrahimi, D. Peddis, M. Parolini, S. Pisani and M. Sturini, Fe_3O_4-halloysite nanotube composites as sustainable adsorbents: Efficiency in ofloxacin removal from polluted waters and ecotoxicity, *Nanomaterials*, 2022, **12**, 4330.

27 G. G. Haciosmanoglu, C. Mejias, J. Martin, J. L. Santos, I. Aparicio and E. Alonso, Antibiotic adsorption by natural and modified clay minerals as designer adsorbents for wastewater treatment: A comprehensive review, *J. Environ. Manage.*, 2022, **317**, 115397.

28 D. Mangla, A. Sharma and S. Ikram, Critical review on adsorptive removal of antibiotics: Present situation, challenges and future perspective, *J. Hazard. Mater.*, 2022, **425**, 127946.

29 D. N. R. de Sousa, S. Insa, A. A. Mozeto, M. Petrovic, T. F. Chaves and P. S. Fadini, Equilibrium and kinetic studies of the adsorption of antibiotics from aqueous solutions onto powdered zeolites, *Chemosphere*, 2018, **205**, 137–146.

30 J. Zhao, X. Yang, G. W. Liang, Z. W. Wang, S. Li, Z. R. Wang and X. Y. Xie, Effective removal of two fluoroquinolone antibiotics by PEG-4000 stabilized nanoscale zero-valent iron supported onto zeolite (PZ-NZVI), *Sci. Total Environ.*, 2020, **710**, 136289.

31 G. Wang, Y.Q. Yi, L.L. Huang, J.L. Wang and Z.Q. Fang, Efficient removal of norfloxacin by biological aerated filters: Effect of zeolite modification and analysis of microbial communities, *J. Water Process Eng.*, 2021, **40**, 101799.

32 I. Braschi, S. Blasioli, L. Gigli, C. E. Gessa, A. Alberti and A. Martucci, Removal of sulfonamide antibiotics from water: evidence of adsorption into an organophilic zeolite Y by its structural modifications, *J. Hazard. Mater.*, 2010, **178**, 218–225.

33 F. Maraschi, M. Sturini, A. Speltini, L. Pretali, A. Profumo, A. Pastorello, V. Kumar, M. Ferretti and V. Caratto, TiO_2-modified zeolites for fluoroquinolones removal from wastewaters and re-use after solar light regeneration, *J. Environ. Chem. Eng.*, 2014, **2**, 2170–2176.

34 M. Sturini, F. Maraschi, A. Cantalupi, L. Pretali, S. Nicolis, D. Dondi, A. Profumo, V. Caratto, E. Sanguineti, M. Ferretti and A. Albini, TiO_2 and N-TiO_2 Sepiolite and Zeolite Composites for Photocatalytic Removal of Ofloxacin from Polluted Water, *Materials*, 2020, **13**, 537.

35 I. Anghel, A. M. Grumezescu, A. G. Anghel, I. Chireac, L. Marutescu, D. E. Mihaiescu and M. C. Chifiriuc, Antibiotic potentiator effect of the natural and synthetic zeolites with well-defined nanopores with possible ENT-clinical applications, *Farmacia*, 2012, **60**, 688–695.

36 L. Angiolini, B. Cohen and A. Douhal, Single Crystal FLIM Characterization of Clofazimine Loaded in Silica-Based Mesoporous Materials and Zeolites, *Int. J. Mol. Sci.*, 2019, **20**, 2859.

37 W. Strzempek, A. Korzeniowska, A. Kowalczyk, W. J. Roth and B. Gil, Detemplated and Pillared 2-Dimensional Zeolite ZSM-55 with Ferrierite Layer Topology as a Carrier for Drugs, *Molecules*, 2020, **25**, 3501.

38 S. Mintova, M. Jaber and V. Valtchev, Nanosized microporous crystals: emerging applications, *Chem. Soc. Rev.*, 2015, **44**, 7207–7233.

39 I. Rubashvili, M. Zautashvili, T. Kordzakhia and L. Eprikashvili, Development and validation of quantitative determination HPLC methods of the fluoroquinolone antibiotics-moxifloxacin hydrochloride and norfloxacin in support of adsorption study on natural zeolites, *Period. Tche Quim.*, 2019, **16**, 10–20.

40 I. Braschi, S. Blasioli, E. Buscaroli, D. Montecchio and A. Martucci, Physicochemical regeneration of high silica zeolite Y used to clean-up water polluted with sulfonamide antibiotics, *J. Environ. Sci.*, 2016, **43**, 302–312.

41 L. Leardini, A. Martucci, I. Braschi, S. Blasioli and S. Quartieri, Regeneration of high-silica zeolites after sulfamethoxazole antibiotic adsorption: a combined in situ high-temperature synchrotron X-ray powder diffraction and thermal degradation study, *Mineral. Mag.*, 2014, **78**, 1141–1159.

42 H. Daghooghi-Mobarakeh, N. Campbell, W. K. Bertrand, T. Kumar, L. Wang, R. Wang, M. Miner and P. E. Phelan, Ultrasound-assisted regeneration of zeolite/water adsorption pair, *Ultrason. Sonochem.*, 2020, **64**, 1050.

43 E. Gionfriddo, Green analytical solutions for sample preparation: solid phase microextraction and related techniques, *Phys. Sci. Rev.*, 2020, 20200006.

44 M. Bañobre-López, A. Teijeiro and J. Rivas, Magnetic nanoparticle-based hyperthermia for cancer treatment, *Rep. Pract. Oncol. Radiother.*, 2013, **18**, 397–400.

45 E. Céspedes, J. M. Byrne, N. Farrow, S. Moise, V. S. Coker, M. Bencsik, J. R. Lloyd and N. D. Telling, Bacterially synthesized ferrite nanoparticles for magnetic hyperthermia applications, *Nanoscale*, 2014, **6**, 12958–12970.

46 M. Peiravi, H. Eslami, M. Ansari and H. Zare-Zardini, Magnetic hyperthermia: Potentials and limitations, *J. Indian Chem. Soc.*, 2022, **99**, 100269.
47 A. B. Bourlinos, R. Zboril and D. Petridis, A simple route towards magnetically modified zeolites, *Microporous Mesoporous Mater.*, 2003, **58**, 155–162.
48 D. Tang, M. Pal, T. Meng, D. Mao and Z. Xue, Synthesis and Applications of Magnetic Zeolites: A Comprehensive Review, *J. Supercond. Novel Magn.*, 2025, **38**, 146.
49 H. Faghihian, M. Moayed, A. Firooz and M. Iravani, Synthesis of a novel magnetic zeolite nanocomposite for removal of Cs+ and Sr2+ from aqueous solution: Kinetic, equilibrium, and thermodynamic studies, *J. Colloid Interface Sci.*, 2013, **393**, 445–451.
50 D. Tang, M. Pal, T. Meng, D. Mao and Z. Xue, Synthesis and Applications of Magnetic Zeolites: A Comprehensive Review, *J. Supercond. Novel Magn.*, 2025, **38**, 146.
51 C. Belviso, E. Agostinelli, S. Belviso, F. Cavalcante, S. Pascucci, D. Peddis, G. Varvaro and S. Fiore, Synthesis of magnetic zeolite at low temperature using a waste material mixture: Fly ash and red mud, *Microporous Mesoporous Mater.*, 2015, **202**, 208–216.
52 C. Belviso, G. Guerra, M. Abdolrahimi, D. Peddis, F. Maraschi, F. Cavalcante, M. Ferretti, A. Martucci and M. Sturini, Efficiency in Ofloxacin antibiotic water remediation by magnetic zeolites formed combining pure sources and wastes, *Processes*, 2021, **9**, 2137.
53 C. Belviso, State-of-the-art applications of fly ash from coal and biomass: A focus on zeolite synthesis processes and issues, *Prog. Energy Combust. Sci.*, 2018, **65**, 109–135.
54 C. Belviso, C. Cannas, N. Pinna, F. Cavalcante, A. Lettino, P. Lotti and G. D. Gatta, Effect of red mud added to zeolite LTA synthesis: Where is Fe in the newly-formed material?, *Microporous Mesoporous Mater.*, 2020, **298**, 110058.
55 A. Danish and A. S. Torres, High-performance geopolymer production using reclaimed fly ash: A sustainable approach to landfilled fly ash management?, *Waste Manage.*, 2025, **204**, 114899.
56 Government of India, Report on fly ash generation at coal/lignite based thermal power stations and its utilization in the country for the year 2021–22, 2022, https://cea.nic.in/wpcontent/uploads/tcd/2022/08/Fly_ash_Generation_and_utilisation_Report_2021_22-1.pdf.
57 M. J. McCarthy, T. Robl and L. J. Csetenyi, Recovery, processing, and usage of wet-stored fly ash, *Coal Combust. Prod. (CCP's)*, 2017, 343–367.
58 S. L. Liu, Y. M. Wang, A. X. Wu, M. Z. Zhang, Z. K. Wang and L. B. Wu, Leaching behavior and curing mechanism of red mud composite filling materials, *Acta Mater. Compositae Sin.*, 2023, **40**, 6736–6746.
59 S. Castiglioni, E. Davoli, F. Riva, M. Palmiotto, P. Camporini, A. Manenti and E. Zuccato, Data on occurrence and fate of emerging contaminants in a urbanised area, *Data Brief*, 2018, **17**, 533–543.
60 M. Parolini, B. De Felice, C. Ferrario, N. Salgueiro-González, S. Castiglioni, A. Finizio and P. Tremolada, Benzoylecgonine exposure induced oxidative stress and altered swimming behavior and reproduction in Daphnia magna, *Environ. Pollut.*, 2018, **232**, 236–244.
61 B. De Felice, M. Sugni, L. Casati and M. Parolini, Molecular, biochemical and behavioral responses of Daphnia magna under long-term exposure to polystyrene nanoplastics, *Environ. Int.*, 2022, **164**, 107264.
62 A. Le Bail, H. Duroy and J. L. Fourquet, *Ab initio* structure determination of LiSbWO6 by X-ray powder diffraction, *Mater. Res. Bull.*, 1988, **23**, 447–452.
63 A. C. Larson and R. B. Von Dreele, *General Structure Analysis System (GSAS) Report LAUR 86-748*, Los Alamos National Laboratory, Los Alamos, 2000.
64 B. H. Toby, EXPGUI, a graphical user interface for GSAS, *J. Appl. Crystallogr.*, 2001, **34**, 210–213. 2001.
65 A. W. Burton, K. Ong, T. Rea and I. Y. Chan, On the estimation of averagecrystallite size of zeolites from the Scherrer equation: a critical evaluation of its application tozeolites with one-dimensional pore systems, *Microporous Mesoporous Mater.*, 2009, **117**, 75–90.
66 J. R. Plaisier, L. Nodari, L. Gigli, E. P. R. S. Miguel, R. Bertoncello and A. Lausi, The X-ray diffraction beamline MCX at Elettra: a case study of non-destructive analysis on stained glass, *Acta IMEKO*, 2017, **6**, 71–75.
67 A. E. Deatsch and E. E. Evans, Heating efficiency in magnetic nanoparticle hyperthermia, *J. Magn. Magn. Mater.*, 2014, **354**, 163–172.
68 C. Belviso, F. Cavalcante, J. H. Huertas, A. Lettino, P. Ragone and S. Fiore, The crystallisation of zeolite (X- and A-type) from fly ash at 25 °C in artificial sea water, *Microporous Mesoporous Mater.*, 2012, **162**, 115–121.
69 C. Belviso, P. Lucini, M. Mancinelli, M. Abdolrahimi, A. Martucci, D. Peddis, F. Maraschi, F. Cvalacante and M. Sturini, Lead, zinc, nickel and chromium ions removal from polluted waters using zeolite formed from bauxite, obsidian and their combination with red mud: Behaviour and mechanisms, *J. Cleaner Prod.*, 2023, **415**, 137814.
70 S. Babić, A. J. M. Horvat, D. P. Mutavdžić and M. Kaštelan-Macan, Determination of pKa values of active pharmaceutical ingredients, *TrAC, Trends Anal. Chem.*, 2007, **26**, 1043–1061.
71 E. Turiel, A. Martín-Esteban and J. L. Tadeo, Multiresidue analysis of quinolones and fluoroquinolones in soil by ultrasonic-assisted extraction in small columns and HPLC-UV, *Anal. Chim. Acta*, 2006, **562**, 30–35.
72 M. Sturini, A. Speltini, F. Maraschi, E. Rivagli and A. Profumo, Solvent-free microwave-assisted extraction of fluoroquinolones from soil and liquid chromatography-fluorescence determination, *J. Chromatogr. A*, 2017, **1217**, 7316–7322.
73 W. J. Atkinson, I. A. Brezovich and D. P. Chakraborty, Usable frequencies in hyperthermia with thermal seeds, *IEEE Trans. Biomed. Eng.*, 1984, **31**, 70–75.
74 I. A. Brezovich, Low frequency hyperthermia: capacitive and ferromagnetic thermoseed methods, *Med. Phys. Monogr.*, 1988, **16**, 82–111.

75 W. W. Wang and Y. J. Zhu, Microwave-Assisted Synthesis of Magnetite Nanosheets in Mixed Solvents of Ethylene Glycol and Water, *Curr. Nanosci.*, 2007, **3**, 171–176.
76 Q. Smith, K. Burnett, N. Saadi, K. Alotaibi, A. Rahman, K. Al-Mayalee and T. Karabacak, Nanostructured antibacterial aluminum foil produced by hot water treatment against *E. coli* in meat, *MRS Adv.*, 2021, **6**, 695–700.
77 R. Eivazzadeh-Keihan, S. Asgharnasl, M. S. Bani, F. Radinekiyan, A. Maleki, M. Mahdavi, P. Babaniamansour, H. Bahreinizad, A. E. Shalan and S. Lanceros-Méndez, Magnetic copper ferrite nanoparticles functionalized by aromatic polyamide chains for hyperthermia applications, *Langmuir*, 2021, **37**, 8847–8854.
78 R. G. Andrade, S. R. Veloso and E. M. Castanheira, Shape anisotropic iron oxide-based magnetic nanoparticles: Synthesis and biomedical applications, *Int. J. Mol. Sci.*, 2020, **21**, 2455.
79 J. Anit, M. G. Praveena, S. Thoufeeq, I. A. Al-Omari and M. R. Anantharaman, A simple polyol one-shot synthesis of Maghemite and Hematite from inexpensive precursors, *Inorg. Chem. Commun.*, 2023, **151**, 110590.
80 N. S. Saadi, L. B. Hassan and T. Karabacak, Metal oxide nanostructures by a simple hot water treatment, *Sci. Rep.*, 2017, **7**, 7158.
81 Q. Smith, K. Burnett, N. Ali, J. Bush and T. Karabacak, Antibacterial efficacy of surface aluminum oxide nanostructures produced by hot water treatment, *Nano Express*, 2023, **4**, 036001.
82 F. Merlo, A. Speltini, F. Maraschi, M. Sturini and A. Profumo, HPLC-MS/MS multiclass determination of steroid hormones in environmental waters after preconcentration on the carbonaceous sorbent HA-C@silica, *Arabian J. Chem.*, 2020, **13**, 4673–4680.

